Impact of Mn/Ni and Li/(Mn+Ni) ratios on phase equilibrium and electrochemical performance of the high voltage spinel LiNi0.5Mn1.5O4

Ilia Tertov, Hunho Kwak, Emmanuelle Suard, Pierre-Etienne Cabelguen, Shinichi Kumakura, François Fauth, Thomas Hansen, Christian Masquelier, Laurence Croguennec

Journal of Power Sources 623 (2024) 235447

Contents lists available at ScienceDirect

Journal of Power Sources

journal homepage: www.elsevier.com/locate/jpowsour

Impact of Mn/Ni and Li/(Mn+Ni) ratios on phase equilibrium and electrochemical performance of the high voltage spinel $LiNi_{0.5}Mn_{1.5}O_4$

Ilia Tertov [a,b,c], HunHo Kwak [d], Emmanuelle Suard [a], Pierre-Etienne Cabelguen [d], Shinichi Kumakura [d], François Fauth [e], Thomas Hansen [a], Christian Masquelier [c,f,g,**], Laurence Croguennec [b,f,*]

[a] Institut Laue-Langevin, 38042, Grenoble, France
[b] Univ. Bordeaux, CNRS, Bordeaux INP, ICMCB UMR 5026, F-33600, Pessac, France
[c] Laboratoire de réactivité et de Chimie des Solides, Université de Picardie Jules Verne, CNRS-UMR 7314, F-80039, Amiens Cedex 1, France
[d] Umicore, 31 Rue du marais, Brussels, BE-1000, Belgium
[e] CELLS-ALBA Synchrotron, Cerdanyola del Vallès, E-08290 Barcelona, Spain
[f] RS2E, Réseau sur le stockage électrochimique de l'énergie, FR CNRS 3459, F-80039, Amiens Cedex 1, France
[g] Institut Universitaire de France, 103 boulevard Saint-Michel, 75005 Paris, France

HIGHLIGHTS

- Large-scale material syntheses (300 g batches) of high-voltage spinel "LiNi0.5Mn1.5O4″
- Impact of the Mn/Ni and Li/(Mn + Ni) ratios and annealing atmosphere on the performance.
- Subtle changes in composition and structure revealed by X-ray and neutron diffraction.
- Sharp comprehension of high-voltage Mn-rich and Li-"poor" spinel-type materials.
- Efficient materials made of sustainable elements for Lithium-ion batteries.

ARTICLE INFO

Keywords:
Li-ion batteries
LNMO
Neutron powder diffraction

ABSTRACT

$LiNi_{0.5}Mn_{1.5}O_4$ (LNMO) emerges as a promising spinel-type positive electrode material for lithium-ion batteries (LIBs) due to its low cost and high operating voltage (4.8 V vs. Li^+/Li), attributed to the $Ni^{4+}/Ni^{3+}/Ni^{2+}$ redox couples, which contribute to high energy density, a crucial requirement for next-generation LIBs. In this study, we investigate the influence of Mn/Ni and Li/(Mn + Ni) ratios on the phase equilibrium and electrochemical performance of LNMO positive electrode materials. A series of 18 samples were synthesized using a two-stage solid-state method with varying Mn/Ni and Li/(Mn + Ni) ratios and annealing under different atmospheres. These synthesis conditions have major impact on the composition and level of purity of LNMO phases, as well as on the nature of the impurities themselves. Mn excess significantly enhances the electrochemical performance, with superior discharge capacity, coulombic efficiency, and capacity retention for the Mn-rich sample with Li/(Mn + Ni) = 0.50. A comprehensive structural analysis combining synchrotron X-ray and neutron powder diffraction gives an in-depth characterization of these samples with a clear differentiation between the global Mn content within samples and that within the LNMO phase.

1. Introduction

$LiNi_{0.5}Mn_{1.5}O_4$ (LNMO) stands out as a highly promising spinel-type positive electrode material for Li-ion batteries (LIBs). Its high operating voltage of 4.8 V vs Li^+/Li, associated with the $Ni^{4+}/Ni^{3+}/Ni^{2+}$ redox couples, provides high energy density, a crucial factor for developing next-generation LIBs [1]. However, the main drawback of LNMO remains its poor cycling stability due to Mn/Ni dissolution [2–4], parasitic

* Corresponding author.
** Corresponding author.
E-mail addresses: christian.masquelier@u-picardie.fr (C. Masquelier), laurence.croguennec@icmcb.cnrs.fr (L. Croguennec).

https://doi.org/10.1016/j.jpowsour.2024.235447
Received 16 July 2024; Received in revised form 2 September 2024; Accepted 10 September 2024
Available online 24 September 2024

surface reactions as a result of irreversible electrolyte degradation [5,6], and self-discharge at charged states [5,7].

LNMO crystallizes in the spinel structural type with different degrees of Mn/Ni ordering. In the disordered LNMO phase ($Fd\bar{3}m$ S.G.) Li^+ cations occupy tetrahedral 8*c* sites while Ni and Mn cations share the same 16*d* octahedral sites. In contrast, in the ideally ordered LNMO phase ($P4_332$ S.G.), Li^+ cations are located at tetrahedral 8*a* sites, and Ni and Mn cations reside at 4*b* and 12*d* octahedral sites, respectively. In several studies, it was shown that disordered LNMO exhibits superior electrochemical performance at high rates and better cycling stability than ordered LNMO [8–12].

Thus, characterizing the Mn/Ni ordering is crucial. Unfortunately, due to the similar scattering power of Mn and Ni, only low-intense superstructure peaks can be observed on the X-ray powder diffraction (XRPD) pattern of ordered LNMO, which limits a quantitative analysis. Fourier-transform infrared (FTIR) and Raman spectroscopies are more sensitive to the Mn/Ni ordering, with more vibration bands present on spectra of the ordered phase due to its lower symmetry [9,13,14]. In Raman spectroscopy for instance, the band at 160 cm^{-1} is especially sensitive and increases with the extent of the Mn/Ni ordering. However, Raman and FTIR spectroscopies provide only qualitative and local information. ^{7}Li Magic Angle Spinning (MAS) NMR spectroscopy can also be applied to distinguish between ordered and disordered LNMO since it can probe differences in the atomic and electronic environment of Li^+ ions. A single environment is expected for perfectly stoichiometric and ordered LNMO, unlike several environments for disordered LNMO. The interpretation of ^{7}Li MAS NMR spectra of LNMO is challenging, but when coupled with DFT calculations it provides an in-depth understanding of Mn/Ni ordering at the local scale [12,14]. In addition, neutron powder diffraction (NPD) is a vital tool for the quantitative analysis of Mn/Ni ordering and composition of LNMO thanks to the significant difference between neutron scattering lengths of Mn, Ni, Li, and O atoms: −3.7, 10.3, −1.9 and 5.8 fm, respectively. Summarizing the results of XRPD, NPD, and electron diffraction [8,10,11], most LNMO samples consist of nanodomains of the ordered phase, within globally disordered primary particles.

Regarding the synthesis of LNMO powders, annealing temperatures above 730 °C generate the disordered LNMO phase, while lower temperatures lead to the formation of the ordered LNMO phase [10,15,16]. On top of that, oxygen release starts at T ≥ 700 °C under air and at T ≥ 720 °C under oxygen, leading to Ni loss from the LNMO spinel phase due to the formation of the Ni-enriched rock salt-based impurity $Li_z(Ni_{0.33}Mn_{0.67})_{1-z}O$ with Mn/Ni = 2/1, compared to Mn/Ni = 3/1 in LNMO. Summarizing the existing literature, phase equilibrium during synthesis can be described by the following equation:

$$LiNi_{0.5}Mn_{1.5}O_4 \rightarrow qLi_z(Ni_{0.33}Mn_{0.67})_{1-z}O + rLiNi_{0.5-w}Mn_{1.5+w}O_4 + sO_2\uparrow$$

Hence, the LNMO spinel phase possesses, in most cases, higher Mn content compared to the overall nominal Mn/Ni ratio in the sample. Therefore, it is important to distinguish between a composition of the LNMO phase and an overall composition of samples. Most of the studies demonstrate that the degree of Mn/Ni ordering depends on the amount of Mn^{3+} cations or Mn content in the crystal structure of LNMO, associated with the presence of rock salt impurities [8,10]. For instance, Pasero et al. [15]. and Cai et al. [16] show that the disordering of Mn and Ni cations and the formation of rock salt impurities start with oxygen release. During the cooling process rock salt impurities disappear due to oxygen intake, indicating reversibility of this phase transition if the cooling process is well mastered. Amatucci et al. [17,18] investigated a series of Mn-rich LNMO samples, $LiNi_xMn_{2-x}O_4$ ($0.36 \leq x \leq 0.50$), and demonstrated, comparing changes in the intensity ratio of two FTIR active bands at 619 cm^{-1} and 588 cm^{-1}, that full Mn/Ni disordering is not observed for $x \geq 0.38$. Moreover, the presence of Mn^{3+} cations (Mn excess) in the crystal structure of LNMO spinel phase was shown to enhance the electronic conductivity and rate capability in lithium batteries [17].

In apparent discrepancy with these results, Aktekin et al. [19,20] recently demonstrated by NPD, Raman, and thermogravimetric analysis that, in the case of a commercial Mn-rich LNMO sample, $LiNi_{0.44}Mn_{1.56}O_4$ (Mn/Ni = 78/22), the disordered phase can be prepared without oxygen deficiency and rock salt impurities. A similar result was recently obtained for stoichiometric LNMO (Mn/Ni = 75/25) prepared in molten salt as a platelet-like sample by Oney et al. [21]. On the contrary to Amatucci et al., Duncan et al. [12] did not find a direct correlation between rate capability and Mn^{3+} content, and assigned better electrochemical performance to the lower degree of Mn/Ni ordering, this one being also evaluated by FTIR in their study of $LiNi_xMn_{2-x}O_4$ ($0.3 \leq x \leq 0.5$) samples.

Despite the research conducted by the authors just mentioned [12, 19–22], few studies have thoroughly investigated LNMO samples with global Mn/Ni ratios different from the stoichiometric one of 3/1 (Mn/Ni = 75/25). Moreover, to the best of our knowledge, there are also no systematic studies on the impact of the Li/(Mn + Ni) ratio on the electrochemical performance of LNMO. These statements as well as apparent conflicting results reported in literature encouraged us to perform a comprehensive analysis of the impacts of Mn/Ni and Li/(Mn + Ni) ratios and annealing atmosphere on phase equilibrium and electrochemical performance of LNMO. We have chosen to focus on a narrower range of compositions obtained by large-scale syntheses (300 g batches), employing advanced Synchrotron X-ray and Neutron powder diffraction techniques to investigate subtle, but critical for the electrochemical performance, changes in composition and crystal structure of the LNMO phase.

Our results show that Mn excess plays an important role in enhancing the structural stability and the electrochemical performance of LNMO. Furthermore, our detailed structural characterization of the best-performing samples reveals that the degree of Mn/Ni ordering does not greatly affect the electrochemical performance of Mn-rich LNMO.

2. Experimental

Synthesis. Large-scale batches, each consisting of 300 g of LNMO positive electrode material, were synthesized via a two-stage solid-state method. In the first stage of the synthesis, $Mn_xNi_{1-x}(OH)_2$ hydroxide precursors (Umicore, Belgium) with similar morphologies and with Mn/Ni ratios of 73/27, 75/25 and 77/23 were mixed with Li_2CO_3 to yield different Li/(Mn + Ni) ratios of 0.47, 0.50 and 0.53. The mixtures were then fired in a muffle furnace at 1050 °C for 12 h under a synthetic air atmosphere with a heating rate of 1 °C/min. Subsequently, the powders were cooled down to room temperature within 12 h (according to the inertia of the furnace used). During the second stage, the prepared batches were divided into two parts: the first part underwent a firing at 725 °C for 12 h under a dry synthetic air atmosphere, and the second part was fired at 725 °C for 12 h under a dry oxygen atmosphere. Both set of samples were cooled to room temperature within 10 h (according to the inertia of the furnace used). The expected chemical compositions and oxidation states of transition metals for the given Li/(Mn + Ni) and Mn/Ni ratio can be found in Table 1.

Materials characterization. The phase compositions of the prepared samples were investigated using synchrotron X-ray powder diffraction (SXRPD). Patterns were collected using the BL04-MSPD beamline (ALBA, Spain) [23] with a wavelength of 0.6206 Å in Debye-Scherrer geometry from samples sealed in 0.7 mm diameter borosilicate glass capillaries. The degree of Mn/Ni ordering was studied by neutron powder diffraction (NPD). Data were collected at the D2B High-Resolution Diffractometer (Institut Laue-Langevin, Grenoble, France) with a wavelength of 1.59 Å in Debye−Scherrer geometry. The samples were loaded in vanadium cylindrical holders of 8 mm diameter. The instrumental profile function of both SXRPD and NPD diffractometers was determined using $Na_2Ca_3Al_2F_{14}$ as a standard sample. Treatment of diffraction data and Rietveld refinements were performed using

Table 1
Expected chemical composition and oxidations state of transition metal cations in LNMO, considering the formation a single spinel phase, for the given Mn/Ni and Li/(Mn + Ni) ratios.

Mn/Ni ratio	Li/(Mn + Ni) ratio	Expected LNMO composition
73/27	0.47	$Li_{0.959}Ni^{2+}_{0.551}Mn^{3+}_{0.020}Mn^{4+}_{1.470}O_4$
	0.5	$LiNi^{2+}_{0.460}Ni^{3+}_{0.080}Mn^{4+}_{1.460}O_4$
	0.53	$Li_{1.039}Ni^{2+}_{0.354}Ni^{3+}_{0.176}Mn^{4+}_{1.431}O_4$
75/25	0.47	$Li_{0.959}Ni^{2+}_{0.510}Mn^{3+}_{0.102}Mn^{4+}_{1.429}O_4$
	0.5	$LiNi^{2+}_{0.500}Mn^{4+}_{1.500}O_4$
	0.53	$Li_{1.039}Ni^{2+}_{0.392}Ni^{3+}_{0.098}Mn^{4+}_{1.471}O_4$
77/23	0.47	$Li_{0.959}Ni^{2+}_{0.469}Mn^{3+}_{0.184}Mn^{4+}_{1.388}O_4$
	0.5	$LiNi^{2+}_{0.460}Mn^{3+}_{0.080}Mn^{4+}_{1.460}O_4$
	0.53	$Li_{1.039}Ni^{2+}_{0.431}Ni^{3+}_{0.020}Mn^{4+}_{1.510}O_4$

the Jana2006 [24] and the FullProf suite software packages [25]. Additional Lorentzian broadening observed for superstructure reflections of the ordered LNMO ($P4_332$ S.G.), present as signature of small antiphase domains, was refined with FullProf using size model #12 [8].

The morphology and distribution of Ni and Mn within particles were studied with a scanning electron microscope (SEM) TESCAN VEGA equipped with an energy-dispersive X-ray (EDX) spectrometer. The particle size distribution (PSD) was measured via laser diffraction on the Bettersizer 2600 Particle Size Analyzer for powders dispersed in water by sonication. The amount of Li, Mn and Ni in the samples was determined by inductively coupled plasma-optical emission spectroscopy (ICP-OES) using the Varian ICP-OES 720 ES. The solutions for the measurements were prepared by dissolution of powders in the 1:1 vol mixture of HCl and HNO_3.

Electrode Preparation and Electrochemical Tests. Electrode composites were prepared by mixing 90 wt. % of active material, 5 wt. % of carbon black (C45, Alfa Aesar, 99.9 %) and 5 wt. % of poly (vinylidene fluoride) (Sigma-Aldrich) in N-methyl-2-pyrrolidone (NMP, Sigma Aldrich, 99.5 %) with 30 wt% of dry matter. The resulting slurries were dried in an oven at 70 °C for 12 h, then the 14 mm diameter electrodes were cut, calendared and dried at 80 °C under a dynamic vacuum for 12 h. The resulting mass loading of the electrodes was 10–11 mg/cm^2. Galvanostatic charge-discharge electrochemical cycling was performed in Al-clad CR2032-type coin cells within the voltage window of 3.0–4.9 V vs. Li^+/Li. The Li metal was used as a counter electrode, the 1M solution of $LiPF_6$ in ethylene carbonate and dimethyl carbonate (EC-DMC, 1:1 vol mixture) was used as an electrolyte, and two layers of Celgard were used as separators. The detailed cycling protocols are described in Table 2.

Table 2
Detailed cycling protocols of LNMO electrodes in half cells versus Li metal. Charge/Discharge rates refer to the theoretical capacity of 147 mA h/g, and for instance C/10 charge rate corresponds to the theoretical exchange of 1 Li^+ in 10 h.

C-rate cycling protocol			
Step	Number of Cycles	Charge rate C	Discharge rate D
1	1	0.1	0.1
2	5	0.25	0.2, 0.5, 1, 2, 3
3	1	0.25	0.1
4	25	0.25	1
5	1	0.25	0.1
6	1	0.25	1
7	25	1	1
Long cycling protocol			
1	100	0.2	0.2

3. Results and discussion

3.1. Exploring the Mn/Ni and Li/(Mn + Ni) composition space

To identify all the phases present in the 18 prepared samples (9 compositions, 2 annealing atmospheres), SXRPD experiments were conducted. For clarity, as examples, only the SXRPD patterns of two specific subsets of composition space are plotted in Fig. 1: samples with a fixed Li/(Mn + Ni) ratio of 0.50 and varying Mn/Ni ratios on one side (Fig. 1a), and samples with a fixed Mn/Ni ratio of 75/25 and varying Li/(Mn + Ni) ratios on the other side (Fig. 1b). To identify impurity phases, a series of theoretical XRPD patterns of spinel ($Li_{0.5}NiMn_{1.5}O_4$), rock salt (Ni_6MnO_8, ICSD # 80301) and layered ($LiNi_{0.7}Mn_{0.3}O_2$, ICSD # 97788) oxides were used, they are plotted in Fig. S3. The refined lattice parameters, phase fractions and types of the impurity phases encountered for all the samples can be found in Fig. 2. Calculated/experimental Rietveld plots after the refinement can be found in Fig. S1. The refined weight fraction of impurity phases and their lattice parameters can be found in Table S1.

Considering the slice of the composition space with a fixed Li/(Mn + Ni) ratio of 0.50 and variable Mn/Ni ratio, it can be seen that the amount of impurity phases decreases with an increase of the Mn/Ni ratio (Fig. 1a), indicating that slight Mn excess significantly improves the structural stability of LNMO. The same tendency is observed also for other Li/(Mn + Ni) ratios (Fig. 2a). Such impact of Mn excess can be explained by the suppression of the formation of Ni-enriched rock salt-based impurities [11,15] due to lower overall Ni concentration in the sample, which shifts the equilibrium towards the formation of the LNMO phase. Annealing under oxygen atmosphere (rather than air, with pO_2 = 20 %) provides a more efficient oxygen intake that results in a decrease of the amount of impurity phases in the samples with Mn/Ni = 73/27 and 75/25 while yielding a pure LNMO sample for Mn/Ni = 77/23. It is worth noting that in all the samples prepared under oxygen, low-intense superstructure reflections (highlighted in grey) of the ordered LNMO (310 and 320) can be observed, suggesting a relatively high degree of Mn/Ni ordering.

Interestingly, in the case of Ni-rich samples (Mn/Ni = 73/27), all the impurity reflections can be described by using rock salt and layered oxide impurity phases, while in the case of 75/25 and 77/23 Mn/Ni ratios only the rock salt structural model describes all the reflections. It can thus be assumed that lower Mn/Ni ratios result in the formation of layered oxide impurities. Determining the chemical compositions of the impurity phases was challenging due to their small phase fractions but the c/a ratio can be used to estimate the degree of Li/M mixing at Li sites in the layered oxide (M being Ni and/or Mn). A c/a ratio close to 5.0 indicates an "ideal layered structure" without Li/M mixing (c/a = 4.99 for $LiCoO_2$, ICSD # 128531) [26]. The experimental c/a ratio of 4.94(2) in the layered oxide impurity phase in the sample with Mn/Ni = 73/27 prepared under air suggests a significant deviation from the ideal 'layered' crystal structure of the layered oxide with an under-stoichiometry in Li. In the slice of composition space with a fixed Mn/Ni ratio of 75/25 and variable Li/(Mn + Ni) ratio, deviations from the ideal Li stoichiometry (Li/(Mn + Ni) = 0.50) lead to significantly higher amounts of impurity phases. Moreover, these deviations alter the type of impurities: spinel-based impurities are observed in the samples with Li/(Mn + Ni) = 0.47 (<0.50), while layered oxide-based impurities are prevalent in the samples with Li/(Mn + Ni) = 0.53 (>0.50) (Fig. 1b). It is noteworthy that for the samples with Li/(Mn + Ni) = 0.47, the disordered spinel with a fixed Li-deficient composition of $Li_{0.5}NiMn_{1.5}O_4$ was used for the Rietveld refinements as the spinel-based impurity phase. The pronounced asymmetry (left shoulders) (Fig. S2, Pattern S7) in the broad reflections of the spinel-based impurity can be attributed to the formation of a series of phases belonging to the solid-solution $Li_xM_{3-x}O_4$ (where x < 1, M = Ni, Mn), with different and larger lattice parameters compared to the main LNMO phase. This asymmetry causes an incorrect description of the profile resulting in unreliable phase

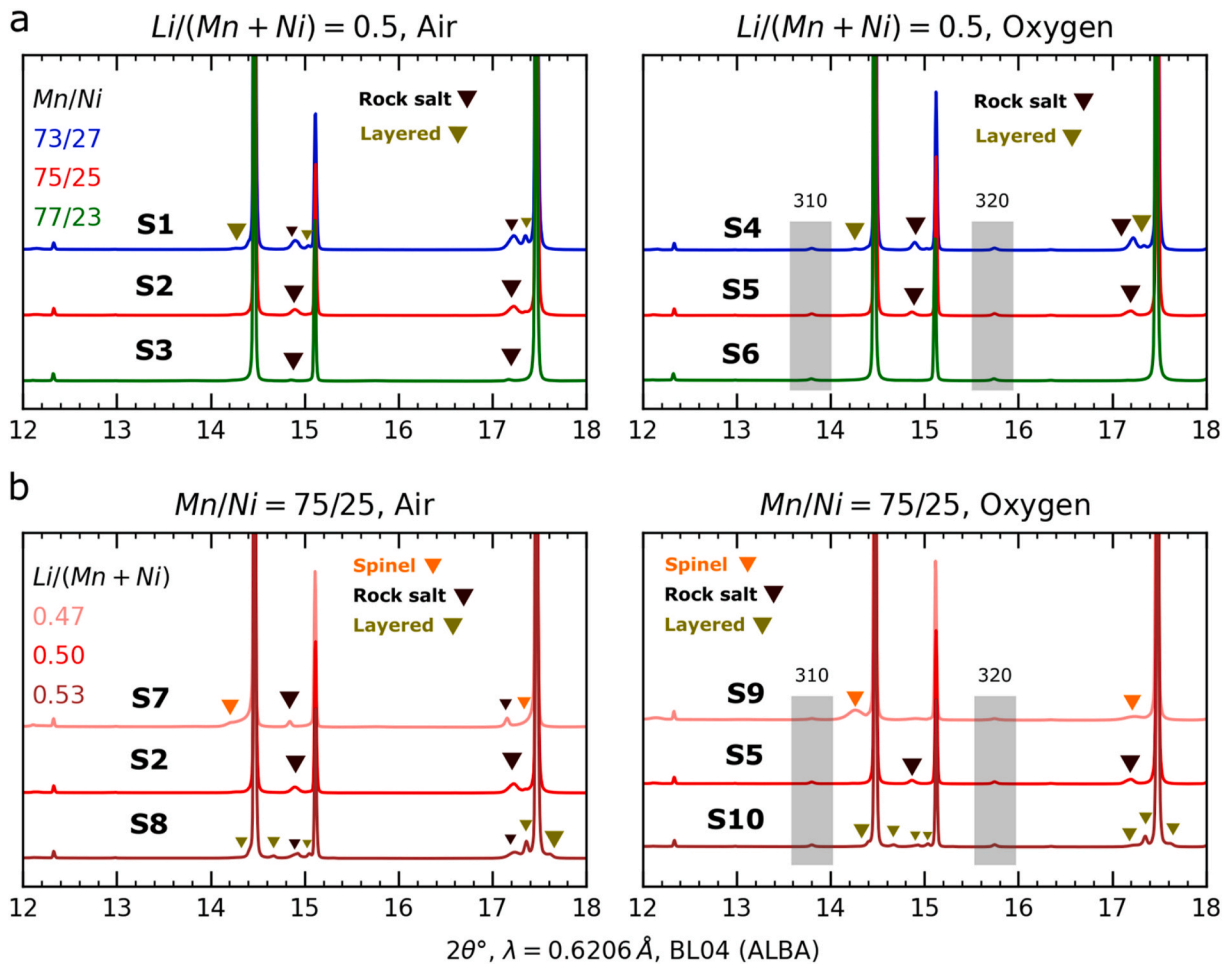

Fig. 1. Selected 2θ° range of SXRPD patterns collected for the samples with Li/(Mn + Ni) = 0.5 and different Mn/Ni ratios (a) and for the samples with Mn/Ni = 75/25 and different Li/(Mn + Ni) ratios (b). The effect of the annealing atmosphere is compared: synthetic air (left) versus oxygen (right). Superstructure reflections of ordered LNMO are highlighted in grey. Corresponding Rietveld plots for chosen samples can be found in Figure S1 and Figure S2 for samples n°1, 4, and 7–10 in 2θ ranges 2–50° and 14–18°, respectively.

fractions of the spinel-based impurity.

The lattice parameter of the LNMO phase is naturally dependent on its composition (stoichiometry) and on the oxidation states of the transition metals M. In the ideal stoichiometric LNMO (Mn/Ni = 75/25 and Li/(Mn + Ni) = 0.50) only Ni^{2+} and Mn^{4+} cations are present. An increase of the Mn/Ni ratio should lead to an increase of the lattice parameter of LNMO as a result of the reduction of Mn^{4+} into Mn^{3+}, which possesses a larger ionic radius of 0.65 Å (in an octahedral environment, i.e. with CN = 6) compared to that of 0.53 Å for Mn^{4+} (with CN = 6). Thus, an increase of the amount of Mn^{3+} cations in the LNMO phase increases its lattice parameter. Indeed, samples with Mn/Ni ratio = 77/23 exhibit the largest lattice parameters (Fig. 2b), indicating the highest amount of Mn^{3+} cations in the LNMO phase.

In the case of Mn/Ni = 73/27 and Li/(Mn + Ni) = 0.50, an oxidation of Ni^{2+} into Ni^{3+} should occur resulting in a significant shrinkage of the LNMO lattice due to the smaller ionic radii of 0.56 Å for Ni^{3+} (with CN = 6), compared to that of 0.69 Å for Ni^{2+} (with CN = 6). However, the presence of Ni^{3+} cations in LNMO has never been reported before. Moreover, from our data we can confirm that it is not happening due to similar lattice parameters of LNMO samples with Mn/Ni = 73/27 and 75/25, indicating rather similar stoichiometry of the LNMO phases. The Ni excess in the samples with Mn/Ni = 73/27 is compensated by the formation of greater amount of the Ni-enriched rock salt-based impurity.

As shown above, the variations of Li/(Mn + Ni) ratio affect the type of impurity phases in the samples and as a consequence change the composition of the LNMO phase. For the samples with Li/(Mn + Ni) = 0.5, the rock salt impurity is mainly observed in the samples. Cabana et al. [11], using transmission electron microscopy and EDX analysis, showed that the rock salt impurity phase possess the Ni-enriched composition $Li_x(Ni_{0.33}Mn_{0.67})_{1-x}O$ with Mn/Ni = 2/1. In other words, the presence of the rock salt impurity increases the amount Mn^{3+} cations in the LNMO phase and its lattice parameters.

An increase of Li/(Mn + Ni) ratio should result in an oxidation of transition metal cations and an incorporation of Li^+ cations into the octahedral sites of the spinel structure, leading to the overall shrinkage of the lattice of LNMO. The same behavior is observed for Li-rich layered oxides and Li-rich spinels $Li_{1+x}Mn_{2-x}O_4$ [27–30]. Indeed, the samples with Li/(Mn + Ni) = 0.53 have smaller lattice parameters, compared to Li/(Mn + Ni) = 0.47 and 0.50, suggesting the possible incorporation of Li cations into octahedral sites. However, the Rietveld refinements of the Li-rich samples did not allow to reveal a significant decrease of electron density at octahedral sites, and hence prevented to conclude firmly. It should be noted that the scattering power of Li is incomparably smaller than the scattering power of Ni and Mn. Our data shows that the overall Li excess in the sample is compensated by the formation of the layered oxide impurity, which has higher Li/M ratio compared with rock salt impurity [31]. Taking into account the presence of the layered oxide impurity in the samples with Mn/Ni = 73/27 and Li/(Mn + Ni) = 0.5 (Fig. 2c), it can be suggested that the layered oxide impurity also has a Ni-enriched composition as the rock salt impurity, so its formation increases Mn content in the LNMO phase and its lattice parameters.

As shown in Fig. 2, Li deficiency in the samples leads to the presence

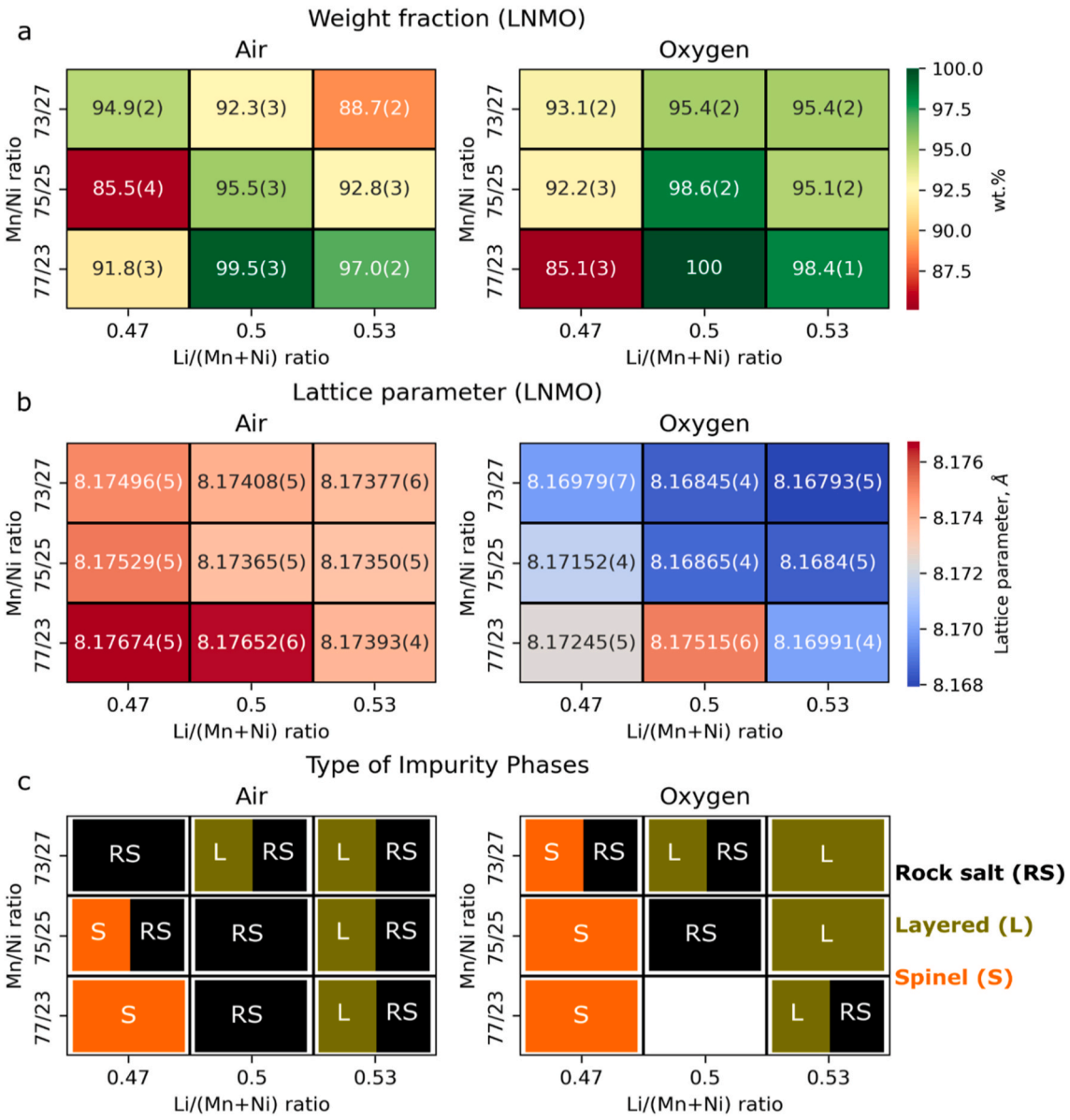

Fig. 2. Weight fraction (a) and lattice parameter (b) of the LNMO phase as determined from the Rietveld refinements from the corresponding SXRPD patterns. The identification of the impurity phases (RS = Rock-Salt, L = Layered, S = Spinel) present next to the LNMO spinel phase and used for the Rietveld refinement is given in (c).

of a spinel-type impurity next to the main spinel phase. Note that a decrease of Li/(Mn + Ni) ratio in the LNMO spinel structure should result in an increase of the lattice parameter due to the reduction of Mn^{4+} cations if the Li deficiency was compensated by the presence of transition metal cations into tetrahedral sites. The Rietveld refinement of the samples with Li/(Mn + Ni) = 0.47 did not reveal a significant increase of electron density at tetrahedral sites. The Li-deficient samples with Mn/Ni ratios of 73/27 and 75/25 systematically exhibit larger lattice parameters for the LNMO spinel phase compared to the samples with a Li/(Mn + Ni) ratio of 0.5. This suggests that the spinel impurity in these samples is Ni-enriched. However, in the sample with a Mn/Ni ratio of 77/23, prepared under oxygen, the lattice parameter of the LNMO phase is smaller than in the sample with a Li/(Mn + Ni) ratio of 0.5. This difference can be attributed to the higher Mn content in the spinel impurity phase. Considering the relatively low weight fraction of the LNMO phase in the sample with a Mn/Ni ratio of 77/23 and a Li/(Mn + Ni) ratio of 0.47 (Fig. 2a), the overall Mn excess and Li deficiency may shift the equilibrium towards forming a spinel impurity with higher Mn content.

In summary, our systematic composition screening study indicates that Mn excess stabilizes the crystal structure of the LNMO spinel by preventing the formation of Ni-enriched rock salt-based impurities. On the other hand, increasing the amount of Ni leads to higher levels of impurity phases and the emergence of layered oxide-based impurities. Variations in Li content – both deficiency and excess – also result in higher amounts of impurities, the nature of impurities changing from spinel oxide-based to layered oxide-based, respectively. Furthermore, annealing in an oxygen atmosphere enhances oxygen intake, which shifts the equilibrium towards the formation of stoichiometric spinel LNMO (Mn/Ni = 75/25 and Li/(Mn + Ni) = 0.50) and decreases the Mn content in the LNMO phase, decreasing its lattice parameters.

3.2. Electrochemical study

Galvanostatic charge-discharge electrochemical cycling was performed for all the 18 samples in the voltage range of 3.0–4.9 V in coin

cells with Li metal as a counter electrode. It should be noted that the prepared electrodes possess relevant mass loadings of 10–11 mg/cm^2. The detailed cycling conditions can be found in Table 2. At least three different coin cells were assembled and tested in parallel for each sample to access reproducibility. The data presented in Fig. 3 represent the average of these three cells for each sample. Confidence intervals were calculated using a normal distribution with the confidence level of 95 %.

It can be seen that the sample with Mn/Ni = 77/23 and Li/(Mn + Ni) = 0.5, prepared under air, demonstrates the highest discharge capacities of 140.21(5) mAh/g and 133.8(9) mAh/g at D/10 (Fig. 3a) and 3D (Fig. 3b) rates respectively, as well as the highest coulombic efficiency of 97.69(7)% (Fig. 3c) in the first cycle, compared to the samples with Mn/Ni = 73/27 and 75/25. The deviation from the ideal Li stoichiometry (Li/(Mn + Ni) = 0.5) results in the deterioration of the electrochemical performance for samples with Mn/Ni = 75/25 and 77/23 prepared under both air and oxygen atmospheres, which can be attributed to the higher amount of impurity phases (Fig. 2a). To our surprise, in the case of the samples with Mn/Ni = 73/27, Li deficiency (Li/(Mn + Ni) = 0.47) leads to higher discharge capacity and coulombic efficiency, compared to the samples with Li/(Mn + Ni) = 0.50 and 0.53.

A careful analysis of the electrochemical and structural data reveals that the discharge capacity at 0.1D rate is strongly related with the weight fraction of the LNMO phase in the samples (Fig. 4a (right)). Higher discharge capacities are achieved for the samples with higher weight fraction of the LNMO phase. In addition, for the same given wt.% of LNMO, the materials with larger lattice parameters exhibit higher discharge capacity (see connecting arrows in Fig. 4).

A clear correlation is also observed between the 3D/0.1D discharge capacity ratio, related to the power performances of the material, and lattice parameters. Higher values of the 3D/0.1D ratio are observed for the samples with larger lattice parameters (Fig. 4b), while no clear trend can be seen with the purity of the samples. It is important to note that all

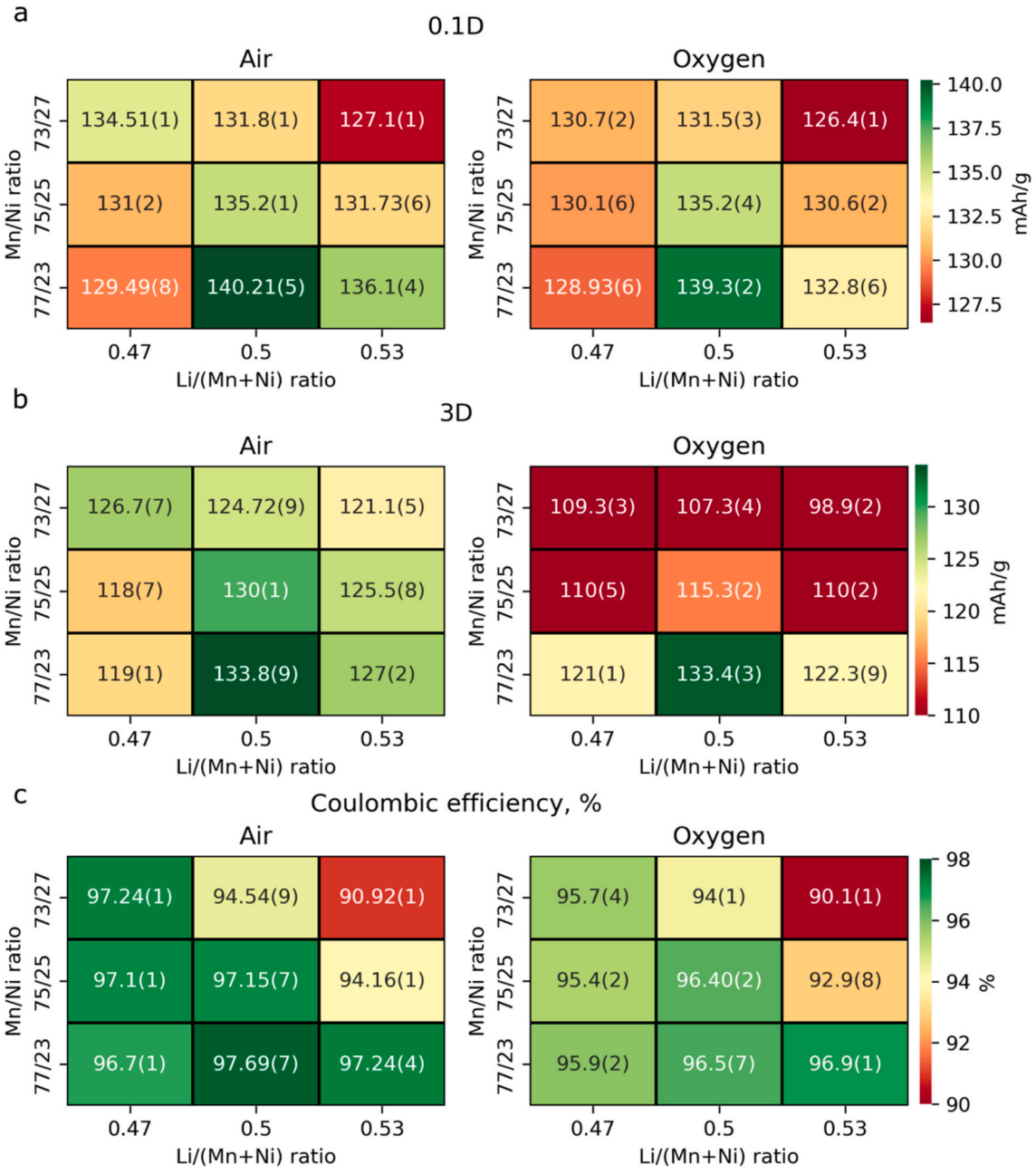

Fig. 3. Discharge capacity at 0.1D (a) and 3D rates (b), and Coulombic efficiency in the first cycle (c) for all the samples. The effect of the annealing atmosphere is compared: synthetic air (left) versus oxygen (right).

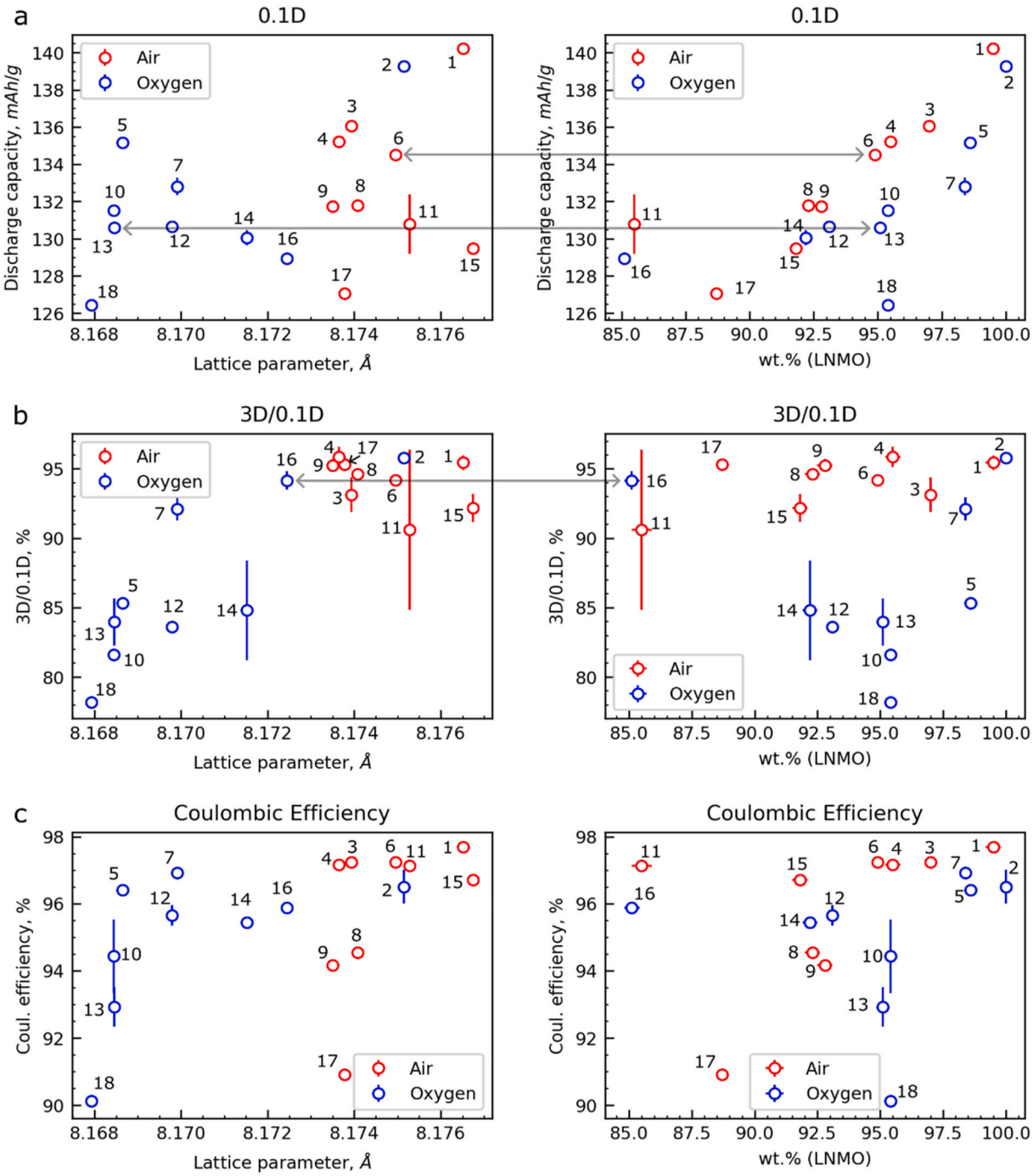

Fig. 4. Discharge capacity at 0.1D rate (a), 3D/0.1D ratio (b) and Coulombic efficiency (c) against lattice parameters (left) and weight fractions (right) of the LNMO phase.

samples prepared under dry air, regardless of the Mn/Ni and Li/(Mn + Ni) ratios, exhibit higher discharge capacities at 0.1D and 3D rates, as well as higher coulombic efficiency in the first cycle compared to samples prepared under oxygen. As mentioned earlier, the lattice parameter of the LNMO phase is highly sensitive to the Mn content in the LNMO phase. Therefore, we can conclude that while the purity of the samples dictates the reversible capacity, the power performance and coulombic efficiency are determined by the lattice parameter, and consequently, the Mn content in the LNMO phase.

3.3. Asymmetry between charge and discharge voltage-composition profiles

A clear asymmetry is observed between charge and discharge curves for all the prepared samples, except those with Mn/Ni = 77/23 and Li (Mn + Ni) = 0.47 and 0.5. For simplicity, only the charge/discharge curves of chosen samples are plotted in Fig. 5 in order to illustrate that asymmetry: with Mn/Ni = 73/27 (Ni-rich) and 77/23 (Mn-rich), and with Li(Mn + Ni) = 0.5 and 0.53. The charge/discharge curves of all the samples with the corresponding derivatives can be found in **Figs. S4–S5**. In the dQ/dV plots of the Ni-rich samples, prepared under air (Fig. 5a), an additional redox process is observed upon charge at ≈ 4.5 V vs. Li^+/

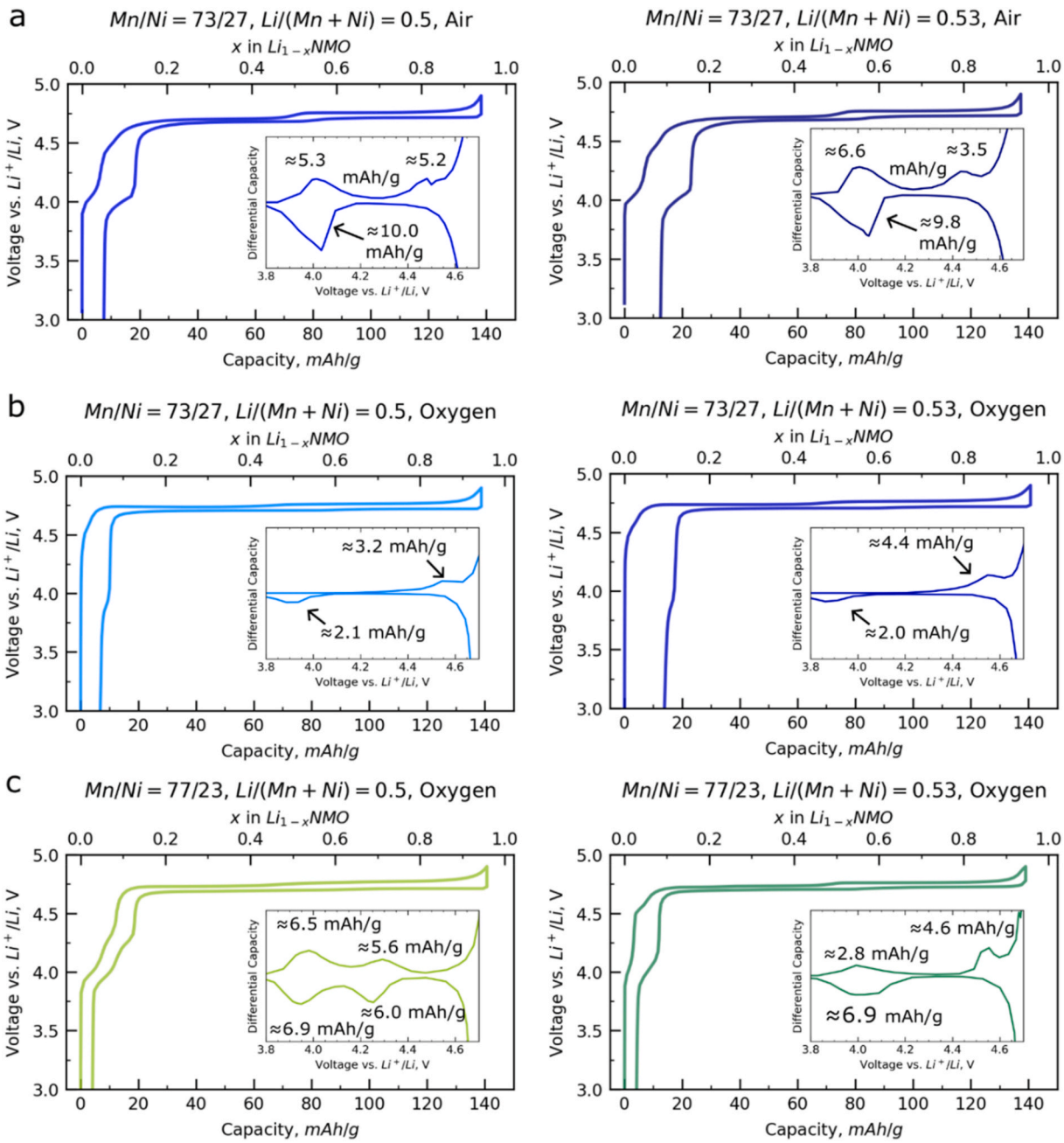

Fig. 5. Charge/discharge curves at 0.1C/0.1D rate of the samples with Mn/Ni = 73/27 and Li(Mn + Ni) = 0.5 (left) and 0.53 (right), prepared under air (a) and oxygen (b). Charge/discharge curves at 0.1C/0.1D rate of the samples with Mn/Ni = 77/23 and Li(Mn + Ni) = 0.5 (left) and 0.53 (right), prepared under oxygen (c).

Li, which is absent in the following discharge, causing asymmetry. The sum of the capacities associated to the redox processes observed upon charging at ≈ 4.0 V and at ≈ 4.5 V vs. Li^+/Li (Fig. 5a, inset), is in good agreement with the capacity recovered during discharge at ≈ 4.0 V vs. Li^+/Li. Therefore, this additional redox process at ≈ 4.5 V may be attributed to the oxidation of a part of the Mn^{3+} cations. However, such a high voltage has never been reported before for the Mn^{4+}/Mn^{3+} redox couple, either in LNMO positive electrode material or in any layered oxide or disordered rock salt materials.

To check for this hypothesis, charge/discharge and dQ/dV curves of the Ni-rich samples prepared under oxygen, with Li(Mn + Ni) = 0.50 and 0.53, were plotted for comparison (Fig. 5b). According to the lowest values of the lattice parameters of the LNMO spinel phases in these samples (Fig. 2b), they hence contain the lowest amount of Mn^{3+} cations in their structure. On the charge curves of these samples, the Mn^{4+}/Mn^{3+} redox process at ≈ 4.0 V is absent, in good agreement with the negligible amount of Mn^{3+} cations in the LNMO spinel phase. However, the redox processes observed at ≈ 4.5 V during charge and at ≈ 4.0 V during discharge are preserved. Therefore, this asymmetry is thus unlikely attributed to the Mn^{4+}/Mn^{3+} redox couple in the LNMO phase.

It is also well-known that Li-rich layered oxides and disordered rock salt materials possess rather similar asymmetry between charge and discharge, in the same voltage range of 4.0–4.5 V vs. Li+/Li and associated to anionic redox phenomena [32–34]. We can thus not fully exclude the presence as such impurities next to the LNMO spinel phase. It is interesting to highlight the absence of this asymmetry in the charge/discharge curves of the Mn-rich samples with Li(Mn + Ni) = 0.5, which does not contain any impurity phases according to SXRPD, whereas it is observed for the Mn-rich samples with Li(Mn + Ni) = 0.53 and containing 1.6 (1) % of impurities (Fig. 5c).

Notably, to the best of our knowledge, this asymmetry has never been reported and observed in the charge/discharge curves of LNMO samples containing similar rock salt and layered oxide impurities [7,9,11,16,30]. It is important to note that in the referenced works, synthesis processes did not include firing steps at temperatures greater than 900 °C, whereas in this study, the first stage of the synthesis involved firing at 1050 °C followed by slow cooling to room temperature. Therefore, it can be suggested that the key to understand this asymmetry phenomenon lies in the initial synthesis stage at 1050 °C. Irreversible phase transformations of the LNMO phase and/or formation of other types of impurities may occur during high-temperature synthesis. However, for example, on the SXRPD pattern of the sample with Mn/Ni = 75/25 and Li(Mn + Ni) = 0.50 after the first stage of the synthesis, the same rock salt impurity is observed, as after the firing at 725 °C during the 2nd stage of the synthesis (Fig. S6). A separated study using in situ temperature-controlled SXRPD and NPD coupled with transmission electron microscopy and Raman spectroscopy is in progress in our group for better understanding of the phase equilibrium during the high-temperature synthesis of LNMO.

3.4. In-depth structural characterization of the best-performing samples

The structural and electrochemical data discussed in the previous sections suggest that the crucial parameter determining the performance of the LNMO materials at high rates is the amount of Mn^{3+} cations (Mn content) in its crystal structure. To thoroughly investigate and discuss this factor, we thus selected the four best-performing samples, i.e with a fixed Li/(Mn + Ni) ratio of 0.50, with Mn/Ni = 75/25 or 77/23, prepared under synthetic air and oxygen atmospheres. These samples are labelled as 75/25 Air, 77/23 Air, 75/25 Oxygen and 77/23 Oxygen in the following. Additionally, we conducted their compositional structural and morphological characterization combining ICP-OES, SEM coupled with EDX, laser diffraction PSD and NPD (Table 3).

Based on SEM and laser diffraction PSD analysis, the selected samples exhibit a similar morphology of large agglomerates composed of smaller truncated octahedral primary particles, as well as uniform particle size distribution (Fig. S7). ICP-OES results, whatever the synthesis conditions, fall within the confidence interval, confirming the targeted Mn/Ni and Li/(Mn + Ni) ratios (Table 3). Nevertheless, EDX elemental mapping (Fig. S8) reveals the presence of Ni-enriched regions within the particles, likely corresponding to the rock salt-type impurity phase as identified in Fig. 2c. As expected, the pure LNMO sample, labelled as "77/23 Oxygen", appears as the most homogeneous one.

Based on our findings, it appears that synthesizing LNMO samples with Mn/Ni = 75/25 without rock-salt-based impurities is extremely challenging. However, as mentioned in the 'Introduction' section, the formation of rock-salt-based impurities is driven by oxygen release, which begins at temperatures of T ≥ 700 °C in an air atmosphere. Therefore, annealing at temperatures lower than the oxygen release temperature shifts the equilibrium towards the formation of the LNMO phase. However, at these lower temperatures, the reaction is slow. For example, Wang et al. [9] reported formation of the pure LNMO sample, according to laboratory XRPD, with Mn/Ni = 75/25, after annealing of the LNMO sample, containing the rock salt impurity, at 600 °C for 4 days. Another way to shift the equilibrium towards the LNMO phase is to increase an oxygen pressure during synthesis: Pasero et al. [15] showed the formation of the single phase LNMO sample (Mn/Ni = 75/25) after annealing of the LNMO sample with impurities under 120 bars of oxygen at 600 °C only for 3 h.

Table 3
ICP-OES and Laser Diffraction PSD results for the selected samples with Li/(Mn + Ni) = 0.50.

Sample	Mn/Ni	Li/(Mn + Ni)	D_{10}	D_{50}	D_{90}
75/25 Air	3.01(1)	0.49(1)	6.08	10.9	18.5
77/23 Air	3.36(1)	0.50(1)	6.62	11.0	18.1
75/25 Oxygen	3.02(1)	0.50(1)	6.17	11.0	18.7
77/23 Oxygen	3.36(1)	0.51(1)	7.15	12.3	20.7

To investigate in-depth the degree of Mn/Ni ordering and stoichiometry of the LNMO phase, the 4 selected samples were studied combining both SXRPD and NPD (Fig. 6). Interestingly, even on the SXRPD patterns, the superstructure peaks of the ordered phase ($P4_332$ S. G.) can be observed in the samples prepared under oxygen, indicating a high degree of Mn/Ni ordering. On the NPD patterns, the superstructure peaks can be easily observed for the samples 77/23 Air, 75/25 Oxygen, and 77/23 Air. For the sample 75/25 Air the superstructure peaks are extremely broad; however, the (210) reflection can be definitely observed.

For the Rietveld refinement of NPD data, a one- or two-phase model was employed, depending on the presence, or not, of the rock salt impurity phase. The ordered model was used to describe the structure of LNMO, while the structural model of Ni_6MnO_8 was implemented for the rock salt impurity. Both Ni and Mn atoms were placed into the 4*b* and 12*d* octahedral sites in the structural model of LNMO to refine its chemical composition $Li(Ni_{0.5-x}Mn_x)_{4b}(Mn_{1.5+y}Ni_y)_{12d}O_4$. To account for the broadening of the superstructure peaks, an additional Lorentzian broadening of these reflections was refined, taking inspiration from the work of Casas-Cabanas et al. [8]. Then, the average size of the ordered domains was calculated using the Scherrer equation and the integral breadth of the Lorentzian broadening. The results after the Rietveld refinement of both NPD and SXRPD data can be found in Table 4, whereas the corresponding plots can be found in Figs. S9–S10, and Figs. S11–S12 for SXRPD and NPD respectively. Detailed information about the refinement procedure, crystallographic and structural parameters for the 77/23 Air sample can be found in Tables S2–S3.

The samples with Mn/Ni = 75/25 prepared under air or oxygen atmospheres possess a Mn-rich composition for LNMO, which can be attributed to the presence of the Ni-enriched rock salt impurity. As discussed earlier, firing under oxygen enhances oxygen intake reducing the amount of impurity phase and Mn (as well as Mn^{3+}) content in the LNMO phase, as observed in the 75/25 Oxygen sample. Moreover, the mixing of Ni and Mn between the 4*b* and 12*d* sites in this sample also decreases after annealing under oxygen. However, the ideal Mn/Ni distribution, with 100 % of Ni at the 4*b* sites and 100 % of Mn at the 12*d* sites, is not achieved. In the case of Mn/Ni = 77/23, the ideal Mn/Ni distribution would place 92 % of Ni at the 4*b* sites. The refined values of the Ni content at the 4*b* site in the 77/23 Air and 77/23 Oxygen samples are very close to this expected distribution, with 89.9(4) % and 89.6(4) %, respectively. Considering the increase of the size of the ordered domains, it can be concluded that firing under oxygen leads to more ordered LNMO samples. This is consistent with previously reported data [8,14,18].

In the case of Mn-rich samples (Mn/Ni = 77/23), an interesting situation is observed as all structural parameters are quite similar, whatever the annealing atmosphere, except for the size of ordered domains. In other words, the composition of the LNMO phase in these 2 samples appears similar, but with different extent of Mn/Ni ordering. However, it should be noted that in the case of Mn/Ni ≈ 3, the overall scattering length of the transition metals M approaches zero, resulting in high errors in the refined overall compositions. Thus, the lattice parameter is more sensitive to the change in the Mn content. Consequently, the Mn content is in fact slightly lower in the 77/23 Oxygen sample, as smaller lattice parameter, compared to the 77/23 Air sample.

It is noteworthy that no disordering of Mn and Ni cations is observed in the samples with Mn/Ni = 77/23. In the recent works by Aktekin et al. [19,20], it was shown that for the Mn/Ni ratio of 78/22, disordered LNMO can be prepared without oxygen deficiency and rock salt-based impurities at T = 710 °C. In other words, the disordering of Mn and Ni cations can be observed before the release of oxygen during the synthesis. Therefore, we may suggest that the Mn content controls the degree of the Mn/Ni ordering in the crystal structure of LNMO, as Mn

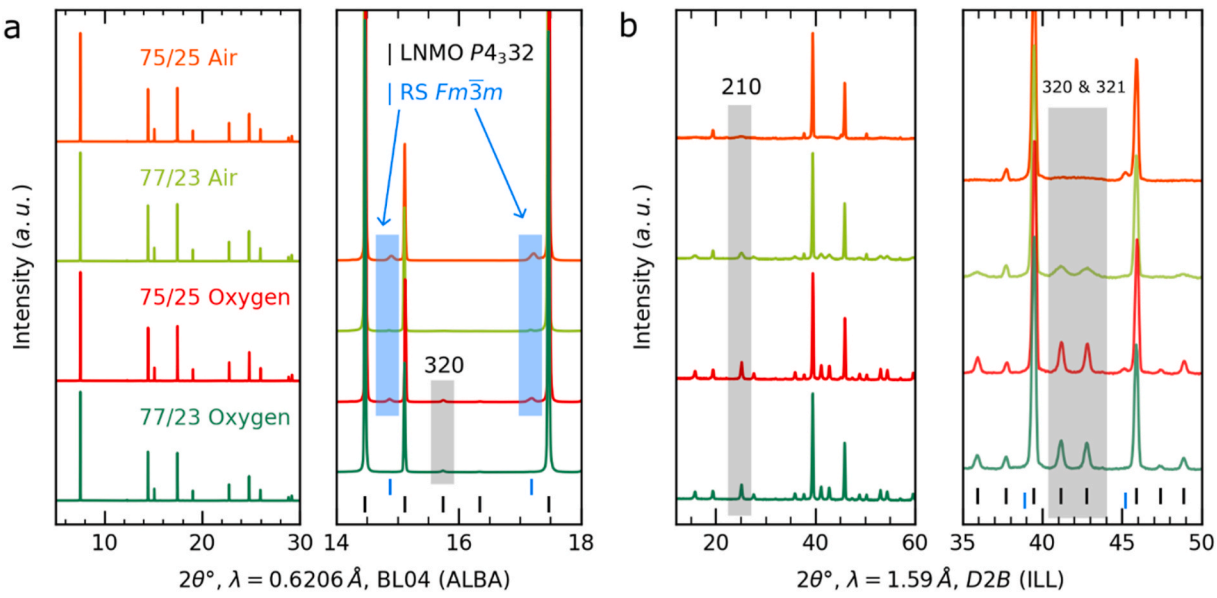

Fig. 6. Selected 2θ° ranges of SXRPD (a) and NPD (b) patterns of 4 selected samples with Bragg positions corresponding to LNMO and Rock salt impurity phases. Some superstructure reflections of ordered LNMO are highlighted in grey. Some reflections of Rock salt impurity are highlighted in light blue. (For interpretation of the references to colour in this figure legend, the reader is referred to the Web version of this article.)

Table 4
Lattice parameters (from SXRPD), weight fractions (from SXRPD) and compositions (from NPD) of the LNMO spinel phase, as well as ordered domain size (from NPD), as obtained for the 4 selected samples after the Rietveld refinement of their SXRPD and NPD data.

Sample	*a(LNMO)*, *Å*	Wt.% (*LNMO*)	*Ni*(4*a*), %	*Mn* (12*d*), %	*Mn/Ni*	Ordered domains size, *nm*
75/25 Air	8.17365(5)	95.5(3)	81(2)	97.2(6)	1.55/0.45(2)	6.5
77/23 Air	8.17652(6)	99.5(3)	89.9(4)	100.0	1.550/0.450(2)	9.3
75/25 Oxygen	8.16865(4)	98.6(2)	93.1(3)	99.6(2)	1.529/0.471(4)	57.6
77/23 Oxygen	8.17515(6)	100	89.6(4)	100.0	1.552/0.448(2)	55.6

excess facilitates Mn/Ni disordering. A separate study using in situ NPD combined with characterization techniques also sensitive to Mn/Ni ordering, such as transmission electron microscopy and Raman spectroscopy, may be of great help to explore the ordering of Mn and Ni cations during synthesis with different initial Mn/Ni ratios, and is in progress in our group.

The charge/discharge electrochemical curves of the 4 selected samples are gathered in Fig. 7. Two distinctive processes can be seen at low-voltage range on the charge/discharge of the samples with Mn/Ni = 77/23, corresponding to the Mn^{4+}/Mn^{3+} redox couple. These processes were reported before by Oney et al. [14], and were assigned to the high degree of Mn/Ni ordering in the prepared samples.

This is in line with our structural data showing no cationic mixing between the 4*b* and 12*d* sites, the latter being fully occupied by Mn (Table 4). In the case of the samples with Mn/Ni = 75/25, the asymmetry between charge and discharge curves is observed with the additional process at ≈ 4.5 V during charging. The possible reasons for this asymmetry were discussed in the previous section, as attributed to the presence of Li-rich layered oxides or disordered rock salt oxides, which exhibit anionic redox behavior with characteristic asymmetry in the voltage range of 4.0–4.5 V vs. Li^+/Li. Our structural data does not allow us to give a clear explanation to this phenomenon. As discussed previously, firing at T = 1050 °C during the 1st stage of the synthesis may cause irreversible structural changes and/or formation of unknown impurity phases, which are preserved during cooling. It is noteworthy that the gained capacity, associated to the process at 4.5 V during charging, is lower in the 75/25 Oxygen sample, corresponding to the lower amount of the impurity phase (Table 4).

3.5. Pivotal role of Mn excess in electrochemical performance of LNMO

According to SXRPD, NPD and ICP-OES results (Tables 3 and 4), a clear distinction can be made between the overall Mn content in the sample and the Mn content specifically incorporated in the LNMO phase. Samples can be ranked in ascending order of Mn content within the LNMO phase as follows: 75/25 Oxygen, 75/25 Air, 77/23 Oxygen, and 77/23 Air.

Observing the capacity retention at high charge/discharge rates (Fig. 8a) and during long cycling protocols (Fig. 8b) of 4 selected samples reveals an increase in capacity retention with a rise in Mn content within the LNMO phase. Notably, the considerable drop in discharge capacities in the 75/25 Oxygen sample correlates with a seemingly lower Mn content and smaller lattice parameter compared to the 75/25 Air, 77/23 Oxygen, and 77/23 Air samples, which exhibit similar Mn content from NPD data and very close lattice parameters (Table 4). Moreover, the similar performances of the 77/23 Air and 77/23 Oxygen samples, despite significantly different sizes of ordered domains, suggest that the Mn content in the LNMO phase plays a more important role than the degree of Mn/Ni ordering.

In literature, reported results suggest that more disordered LNMO samples outperform ordered LNMO samples in terms of electrochemical behavior and most studies have focused on stoichiometric LNMO with a global Mn/Ni ratio of 75/25 [7–10,25]. Disordered LNMO samples, prepared at higher temperatures, tend to contain Ni-enriched rock salt impurities due to oxygen release, resulting in a higher Mn/Ni ratio in the LNMO phase compared to the global ratio of 75/25. Conversely, ordered LNMO samples, typically prepared at lower temperatures under an oxygen atmosphere, contain fewer Ni-enriched rock salt impurities and exhibit Mn/Ni ratios closer to 75/25. Limited studies have thoroughly

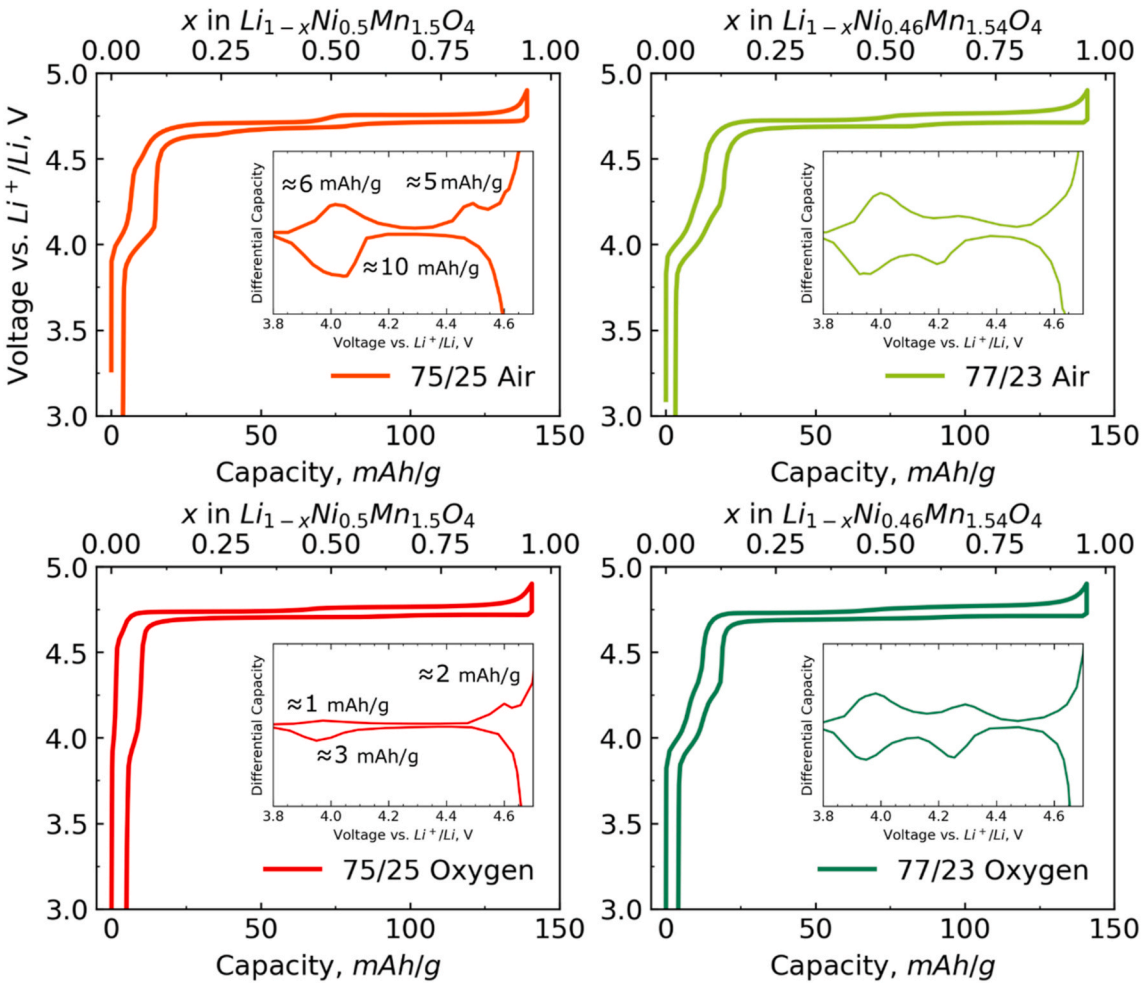

Fig. 7. Charge/Discharge curves in the first cycle at 0.1C/0.1D rates (inset: zoom of the dQ/dV plots in the voltage range of the Mn^{4+}/Mn^{3+} redox couple).

investigated samples with a global Mn/Ni ratio greater than 75/25.

Amatucci et al. [18,19] demonstrated that global Mn excess in samples enhances the electronic conductivity and rate capability of LNMO, attributing the improvement to Mn excess rather than to the degree of Mn/Ni ordering. Conversely, Duncan et al. [11] showed that Mn/Ni disordering improves rate capability irrespective of the Mn content in the LNMO phase. Our data supports the idea that Mn excess plays a more significant role in enhancing electrochemical performance than the degree of Mn/Ni ordering.

It is important to note that a global Mn excess in the LNMO sample results in the presence of Mn^{3+} cations at Ni sites (4*a*) in the crystal structure of the LNMO phase, preventing the ideally ordered crystal structure with perfect Mn/Ni cation ordering between 4*b* and 12*d* sites. This raises questions about the local structure and chemical composition of ordered domains in Mn-rich LNMO. Assuming that ordered domains exhibit perfect Mn/Ni ordering or Mn/Ni = 3, Mn-rich LNMO should consist of at least two types of domains at the particle level: (i) ordered domains with ideal Mn/Ni = 3 and (ii) disordered domains with Mn/Ni > 3. In the case of a global Mn/Ni ratio of 77/23, the Mn/Ni ratio in disordered domains should exceed 77/23. A further study still in progress and utilizing local techniques such as transmission electron microscopy and/or ^{7}Li MAS NMR spectroscopy will help to clarify the distribution and composition of ordered and disordered domains at the single particle level, which could be pivotal in understanding the superior performance of Mn-rich LNMO.

4. Conclusions

In this study, we systematically explored the impact of both Mn/Ni and Li/(Mn + Ni) ratios on phase equilibrium during synthesis and electrochemical performance of LNMO positive electrode materials. We prepared a series of 18 300 g-batches of LNMO using two-stage solid-state method involving high-temperature annealing at 1050 °C followed by low-temperature annealing at 725 °C under both air and oxygen atmospheres.

Our experiments demonstrate that a Mn/Ni ratio of 77/23 (Mn excess) stabilizes the crystal structure of LNMO by suppressing the formation of Ni-enriched rock salt-based impurities. Conversely, a Mn/Ni ratio of 73/27 (Ni excess) results in higher amounts of impurity phases and in the formation of layered oxide-based impurities. Both Li deficiency and Li excess, compared to the ideal Li stoichiometry (Li/(Mn + Ni) = 0.5), lead to higher amount of impurity phases with the type of impurities changing from spinel oxide-based to the layered oxide-based, respectively. Additionally, firing under an oxygen atmosphere provides more efficient oxygen intake shifting the equilibrium towards the formation of LNMO as a spinel-type single phase.

Furthermore, our results enlight the critical role of Mn excess in enhancing the electrochemical performance of LNMO, given that all the prepared samples had a similar microstructure. Mn-rich samples (Mn/Ni = 77/23) exhibit superior discharge capacity, coulombic efficiency and capacity retention at high rates, compared to the stoichiometric samples (Mn/Ni = 75/25). Moreover, our structural characterization suggests that the size of the ordered domains (the degree of Mn/Ni ordering) did not significantly affect the electrochemical performance as

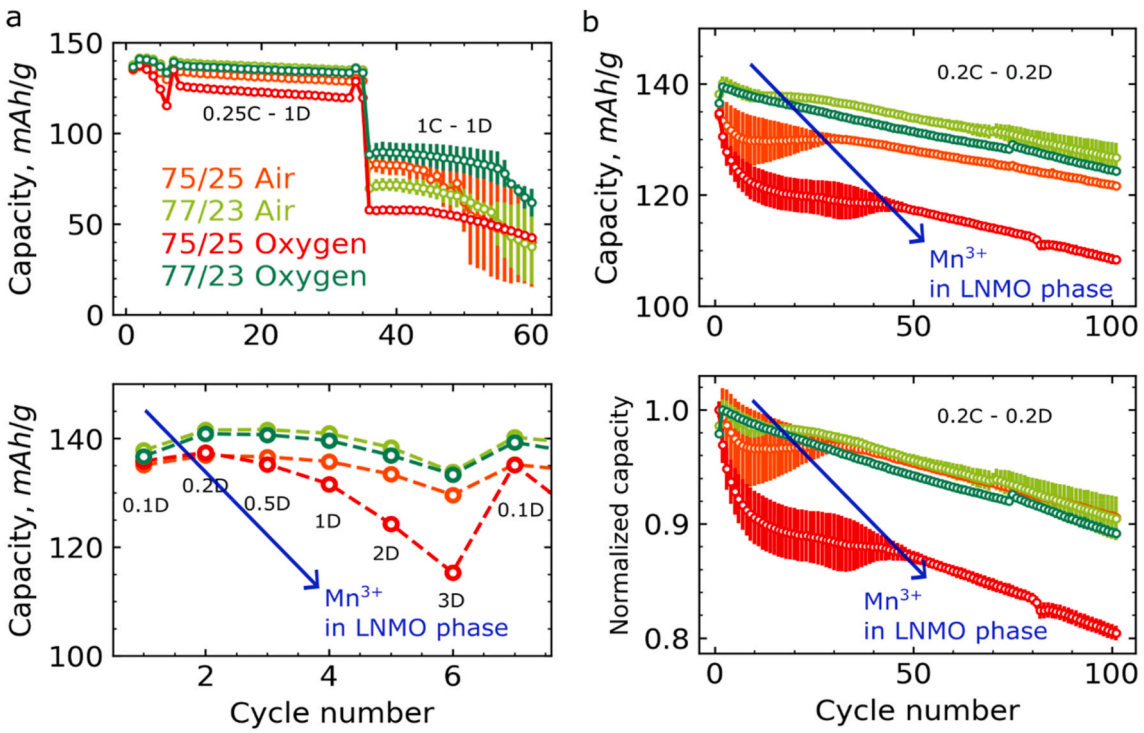

Fig. 8. Capacity retention for the 4 selected samples during the C-rate (a) and long cycling(b) protocols. The detailed description of the cycling programs can be found in Table 2.

the Mn content in the LNMO phase.

In conclusion, our findings highlight the importance of Mn excess in LNMO for achieving superior electrochemical performance. Future research should focus on the impact of Mn excess on the local structure and distribution of the ordered and disordered domains at the single particle level. A comprehensive understanding of the local structure of Mn-rich LNMO is essential for optimizing its electrochemical performance.

CRediT authorship contribution statement

Ilia Tertov: Writing – review & editing, Writing – original draft, Visualization, Validation, Methodology, Investigation, Formal analysis, Data curation, Conceptualization. **HunHo Kwak:** Writing – review & editing, Methodology, Investigation, Data curation. **Emmanuelle Suard:** Writing – review & editing, Validation, Supervision, Methodology, Investigation, Funding acquisition. **Pierre-Etienne Cabelguen:** Writing – review & editing, Validation, Project administration, Methodology, Investigation, Conceptualization. **Shinichi Kumakura:** Writing – review & editing, Methodology, Investigation. **François Fauth:** Writing – review & editing, Methodology, Investigation. **Thomas Hansen:** Writing – review & editing, Methodology, Investigation, Funding acquisition. **Christian Masquelier:** Writing – review & editing, Validation, Supervision, Methodology, Investigation, Funding acquisition, Conceptualization. **Laurence Croguennec:** Writing – review & editing, Validation, Supervision, Project administration, Methodology, Investigation, Funding acquisition, Conceptualization.

Declaration of competing interest

The authors declare the following financial interests/personal relationships which may be considered as potential competing interests:

Croguennec, Masquelier, Tertov reports financial support was provided by Umicore. If there are other authors, they declare that they have no known competing financial interests or personal relationships that could have appeared to influence the work reported in this paper.

Data availability

Data will be made available on request.

Acknowledgements

The authors thank Emmanuel Petit, Cathy Denage, Jérôme Kalisky and Eric Lebraud from ICMCB for their technical support. The authors acknowledge ILL (Grenoble, France) for neutron powder diffraction experiments on the D2B beamline (DOI:10.5291/ILL-DATA.5-24-691), as well as ALBA (Barcelona, Spain) for synchrotron X-ray powder diffraction experiments on the MSPD beamline (proposal 2022097144). They thank the European Union's Horizon 2020 research and InnovaXN programme under the Marie Skłodowska-Curie grant agreement No. 847439 and ILL for the funding of I. Tertov PhD thesis, as well as Umicore, the Région Nouvelle Aquitaine and the French National Research Agency (STORE-EX Labex Project ANR-10-LABX-76-01) for the financial support of their research.

Appendix A. Supplementary data

Supplementary data to this article can be found online at https://doi.org/10.1016/j.jpowsour.2024.235447.

References

[1] G. Liang, V.K. Peterson, K.W. See, Z. Guo, W.K. Pang, Developing high-voltage spinel LiNi0.5Mn1.5O4 cathodes for high-energy-density lithium-ion batteries: current achievements and future prospects, J. Mater. Chem. A 8 (2020) 15373–15398, https://doi.org/10.1039/D0TA02812F.

[2] L. Hanf, J. Henschel, M. Diehl, M. Winter, S. Nowak, Mn2+ or Mn3+ ? Investigating transition metal dissolution of manganese species in lithium ion battery electrolytes by capillary electrophoresis, Electrophoresis 41 (2020) 697–704, https://doi.org/10.1002/elps.201900443.

[3] J. Ma, P. Hu, G. Cui, L. Chen, Surface and interface issues in spinel LiNi0.5Mn1.5O4 : insights into a potential cathode material for high energy density lithium ion batteries, Chem. Mater. 28 (2016) 3578–3606, https://doi.org/10.1021/acs.chemmater.6b00948.

[4] N.R. Park, Y. Li, W. Yao, M. Zhang, B. Han, C. Mejia, B. Sayahpour, R. Shimizu, B. Bhamwala, B. Dang, S. Kumakura, W. Li, Y.S. Meng, Understanding the role of lithium borate as the surface coating on high voltage single crystal LiNi0.5Mn1.5O4, Adv. Funct. Mater. 34 (2024) 2312091, https://doi.org/10.1002/adfm.202312091.

[5] J.W. Kim, D.H. Kim, D.Y. Oh, H. Lee, J.H. Kim, J.H. Lee, Y.S. Jung, Surface chemistry of LiNi0.5Mn1.5O4 particles coated by Al2O3 using atomic layer deposition for lithium-ion batteries, J. Power Sources 274 (2015) 1254–1262, https://doi.org/10.1016/j.jpowsour.2014.10.207.

[6] L. Yang, B. Ravdel, B.L. Lucht, Electrolyte reactions with the surface of high voltage LiNi0.5Mn1.5O4 cathodes for lithium-ion batteries, Electrochem. Solid State Lett. 13 (2010) A95, https://doi.org/10.1149/1.3428515.

[7] X. Liao, Q. Huang, S. Mai, X. Wang, M. Xu, L. Xing, Y. Liao, W. Li, Self-discharge suppression of 4.9 V LiNi0.5Mn1.5O4 cathode by using tris(trimethylsilyl)borate as an electrolyte additive, J. Power Sources 272 (2014) 501–507, https://doi.org/10.1016/j.jpowsour.2014.08.117.

[8] M. Casas-Cabanas, C. Kim, J. Rodríguez-Carvajal, J. Cabana, Atomic defects during ordering transitions in LiNi0.5Mn1.5O4 and their relationship with electrochemical properties, J. Mater. Chem. A 4 (2016) 8255–8262, https://doi.org/10.1039/C6TA00424E.

[9] L. Wang, H. Li, X. Huang, E. Baudrin, A comparative study of Fd-3m and P4332 "LiNi0.5Mn1.5O4,", Solid State Ionics 193 (2011) 32–38, https://doi.org/10.1016/j.ssi.2011.04.007.

[10] J.-H. Kim, A. Huq, M. Chi, N.P.W. Pieczonka, E. Lee, C.A. Bridges, M.M. Tessema, A. Manthiram, K.A. Persson, B.R. Powell, Integrated nano-domains of disordered and ordered spinel phases in LiNi0.5Mn1.5O4 for Li-ion batteries, Chem. Mater. 26 (2014) 4377–4386, https://doi.org/10.1021/cm501203r.

[11] J. Cabana, M. Casas-Cabanas, F.O. Omenya, N.A. Chernova, D. Zeng, M. S. Whittingham, C.P. Grey, Composition-structure relationships in the Li-ion battery electrode material LiNi0.5Mn1.5O4, Chem. Mater. 24 (2012) 2952–2964, https://doi.org/10.1021/cm301148d.

[12] H. Duncan, B. Hai, M. Leskes, C.P. Grey, G. Chen, Relationships between Mn 3+ content, structural ordering, phase transformation, and kinetic properties in LiNixMn2–xO4 cathode materials, Chem. Mater. 26 (2014) 5374–5382, https://doi.org/10.1021/cm502607v.

[13] L. Boulet-Roblin, C. Villevieille, P. Borel, C. Tessier, P. Novák, M. Ben Yahia, Versatile approach combining theoretical and experimental aspects of Raman spectroscopy to investigate battery materials: the case of the LiNi0.5Mn1.5O4 spinel, J. Phys. Chem. C 120 (2016) 16377–16382, https://doi.org/10.1021/acs.jpcc.6b04155.

[14] G. Oney, J. Serrano-Sevillano, M. Ben-Yahia, J. Olchowka, E. Suard, F. Weill, A. Demortiere, M. Casas-Cabanas, L. Croguennec, D. Carlier, Identification of degree of ordering in spinel LiNi0.5Mn1.5O4 through NMR and Raman spectroscopies supported by theoretical calculations, SSRN Journal (2024), https://doi.org/10.2139/ssrn.4711856.

[15] D. Pasero, N. Reeves, V. Pralong, A.R. West, Oxygen nonstoichiometry and phase transitions in LiMn1.5Ni0.5O4−δ, J. Electrochem. Soc. 155 (2008) A282, https://doi.org/10.1149/1.2832650.

[16] L. Cai, Z. Liu, K. An, C. Liang, Unraveling structural evolution of LiNi0.5Mn1.5O4 by in situ neutron diffraction, J. Mater. Chem. A 1 (2013) 6908, https://doi.org/10.1039/c3ta00145h.

[17] M. Kunduraci, J.F. Al-Sharab, G.G. Amatucci, High-power nanostructured LiMn2-xNixO4 high-voltage lithium-ion battery electrode materials: electrochemical impact of electronic conductivity and morphology, Chem. Mater. 18 (2006) 3585–3592, https://doi.org/10.1021/cm060729s.

[18] M. Kunduraci, G.G. Amatucci, Effect of oxygen non-stoichiometry and temperature on cation ordering in LiMn2−xNixO4 (0.50≥x≥0.36) spinels, J. Power Sources 165 (2007) 359–367, https://doi.org/10.1016/j.jpowsour.2006.11.051.

[19] B. Aktekin, M. Valvo, R.I. Smith, M.H. Sørby, F. Lodi Marzano, W. Zipprich, D. Brandell, K. Edström, W.R. Brant, Cation ordering and oxygen release in LiNi0.5–xMn1.5+xO4–y (LNMO): in situ neutron diffraction and performance in Li ion full cells, ACS Appl. Energy Mater. 2 (2019) 3323–3335, https://doi.org/10.1021/acsaem.8b02217.

[20] B. Aktekin, F. Massel, M. Ahmadi, M. Valvo, M. Hahlin, W. Zipprich, F. Marzano, L. Duda, R. Younesi, K. Edström, D. Brandell, How Mn/Ni ordering controls electrochemical performance in high-voltage spinel LiNi0.44Mn1.56O4 with fixed oxygen content, ACS Appl. Energy Mater. 3 (2020) 6001–6013, https://doi.org/10.1021/acsaem.0c01075.

[21] G. Oney, J. Olchowka, A. Demortière, F. Weill, L. Croguennec, Molten salt synthesis of multifaceted pure-phase spinel LiNi0.5Mn1.5O4 platelets, ACS Appl. Energy Mater. 6 (2023) 8189–8196, https://doi.org/10.1021/acsaem.3c01328.

[22] B. Aktekin, M.J. Lacey, T. Nordh, R. Younesi, C. Tengstedt, W. Zipprich, D. Brandell, K. Edström, Understanding the capacity loss in LiNi0.5Mn1.5O4 – Li4Ti5O12 lithium-ion cells at ambient and elevated temperatures, J. Phys. Chem. C 122 (2018) 11234–11248, https://doi.org/10.1021/acs.jpcc.8b02204.

[23] F. Fauth, R. Boer, F. Gil-Ortiz, C. Popescu, O. Vallcorba, I. Peral, D. Fullà, J. Benach, J. Juanhuix, The crystallography stations at the Alba synchrotron, Eur. Phys. J. A 130 (2015) 160, https://doi.org/10.1140/epjp/i2015-15160-y.

[24] V. Petříček, M. Dušek, L. Palatinus, Crystallographic computing system JANA2006: general features, Z. für Kristallogr. - Cryst. Mater. 229 (2014) 345–352, https://doi.org/10.1515/zkri-2014-1737.

[25] J. Rodríguez-Carvajal, Recent advances in magnetic structure determination by neutron powder diffraction, Phys. B Condens. Matter 192 (1993) 55–69, https://doi.org/10.1016/0921-4526(93)90108-I.

[26] M. Bianchini, M. Roca-Ayats, P. Hartmann, T. Brezesinski, J. Janek, There and back again—the journey of LiNiO2 as a cathode active material, Angew. Chem. Int. Ed. 58 (2019) 10434–10458, https://doi.org/10.1002/anie.201812472.

[27] C. Yin, Z. Wei, M. Zhang, B. Qiu, Y. Zhou, Y. Xiao, D. Zhou, L. Yun, C. Li, Q. Gu, W. Wen, X. Li, X. Wen, Z. Shi, L. He, Y. Shirley Meng, Z. Liu, Structural insights into composition design of Li-rich layered cathode materials for high-energy rechargeable battery, Mater. Today 51 (2021) 15–26, https://doi.org/10.1016/j.mattod.2021.10.020.

[28] M. Bianchini, E. Suard, L. Croguennec, C. Masquelier, Li-rich Li1+xMn2–xO4 spinel electrode materials: an operando neutron diffraction study during Li + extraction/insertion, J. Phys. Chem. C 118 (2014) 25947–25955, https://doi.org/10.1021/jp509027g.

[29] C. Masquelier, M. Tabuchi, K. Ado, R. Kanno, Y. Kobayashi, Y. Maki, O. Nakamura, J.B. Goodenough, Chemical and magnetic characterization of spinel materials in the LiMn2O4–Li2Mn4O9–Li4Mn5O12 System, J. Solid State Chem. 123 (1996) 255–266, https://doi.org/10.1006/jssc.1996.0176.

[30] R.J. Gummow, A. de Kock, M.M. Thackeray, Improved capacity retention in rechargeable 4 V lithium/lithium-manganese oxide (spinel) cells, Solid State Ionics 69 (1994) 59–67, https://doi.org/10.1016/0167-2738(94)90450-2.

[31] E. McCalla, J.R. Dahn, The spinel and cubic rocksalt solid-solutions in the Li–Mn–Ni oxide pseudo-ternary system, Solid State Ionics 242 (2013) 1–9, https://doi.org/10.1016/j.ssi.2013.04.003.

[32] A.M. Abakumov, S.S. Fedotov, E.V. Antipov, J.-M. Tarascon, Solid state chemistry for developing better metal-ion batteries, Nat. Commun. 11 (2020) 4976, https://doi.org/10.1038/s41467-020-18736-7.

[33] R.A. House, J.-J. Marie, M.A. Pérez-Osorio, G.J. Rees, E. Boivin, P.G. Bruce, The role of O2 in O-redox cathodes for Li-ion batteries, Nat. Energy 6 (2021) 781–789, https://doi.org/10.1038/s41560-021-00780-2.

[34] R.J. Clément, Z. Lun, G. Ceder, Cation-disordered rocksalt transition metal oxides and oxyfluorides for high energy lithium-ion cathodes, Energy Environ. Sci. 13 (2020) 345–373, https://doi.org/10.1039/C9EE02803J.